

# Nanoscale

Accepted Manuscript



This is an *Accepted Manuscript*, which has been through the Royal Society of Chemistry peer review process and has been accepted for publication.

*Accepted Manuscripts* are published online shortly after acceptance, before technical editing, formatting and proof reading. Using this free service, authors can make their results available to the community, in citable form, before we publish the edited article. We will replace this *Accepted Manuscript* with the edited and formatted *Advance Article* as soon as it is available.

You can find more information about *Accepted Manuscripts* in the [Information for Authors](#).

Please note that technical editing may introduce minor changes to the text and/or graphics, which may alter content. The journal's standard [Terms & Conditions](#) and the [Ethical guidelines](#) still apply. In no event shall the Royal Society of Chemistry be held responsible for any errors or omissions in this *Accepted Manuscript* or any consequences arising from the use of any information it contains.

## ARTICLE

# High-resolution and large-area nanoparticle arrays using EUV interference lithography

Cite this: DOI: 10.1039/x0xx00000x

Waiz Karim <sup>a, b</sup>, Simon Andreas Tschupp <sup>c</sup>, Mehtap Oezaslan <sup>c, d</sup>, Thomas Justus Schmidt <sup>c, e</sup>, Jens Gobrecht <sup>a</sup>, Jeroen Anton van Bokhoven <sup>b, f, \*\*</sup>, Yasin Ekinici <sup>a, \*</sup>

Received 00th January 2012,

Accepted 00th January 2012

DOI: 10.1039/x0xx00000x

[www.rsc.org/](http://www.rsc.org/)

Well-defined model systems are needed for better understanding of the relationship between optical, electronic, magnetic, and catalytic properties of these nanoparticles and their structure. Chemical synthesis of metal nanoparticles results in large size and shape dispersion and lack of lateral order. In contrast, conventional top-down lithography techniques provide control over the lateral order and dimensions. However, they are either limited in resolution or have low throughput and therefore do not enable the large patterning area needed to obtain good signal-to-noise ratio in common analytical and characterization techniques. Extreme ultraviolet (EUV) lithography has the throughput and simplicity advantages of photolithography as well as high resolution due to its wavelength. Using EUV achromatic Talbot lithography, we have obtained 15 nm particle arrays with a periodicity of about 100 nm over an area of several square centimeters with high-throughput enabling the use of nanotechnology for fabrication of model systems to study large ensembles of well-defined identical nanoparticles with a density of  $10^{10}$  particles/cm<sup>2</sup>.

## A. Introduction

Metal nanostructures are of interest due to their unique optical, electronic, magnetic, and catalytic properties <sup>1-3</sup>. For instance, metal nanoparticles play a major role in biomass conversion, in production of chemicals, in the refinery and in fuel cells. Conventional processes that involve chemical synthesis to fabricate model systems either do not feature uniformity in size or lack well-defined separation of nanoparticles over large area <sup>4-6</sup>. Nanopatterning using top-down methods has, therefore, attracted substantial attention to develop reproducible model systems in which size and order of nanoparticles can be controlled in a straightforward manner. Well-defined systems with metal nanoparticles will enable more systematic studies of the effects of particle size, inter-particle distance, and metal-support interaction. Recent advances in nanotechnology have enabled feature sizes below 20 nm, which coincides with particle sizes of interest for applications in optoelectronics <sup>7</sup>, plasmonics <sup>8</sup>, magnetism <sup>9</sup>, and catalysis <sup>10-13</sup>. For example, model catalysts have been fabricated using top-down lithography, such as electron beam lithography (EBL) and photolithography with control of nanoparticle size, surface structure, location, and support-metal interface <sup>14-16</sup>. These conventional techniques are either low-throughput, e.g. EBL, or do not enable the required resolution, e.g. laser interference lithography. Large arrays of nanoparticles have been fabricated using other techniques, such as nano-imprint lithography <sup>17</sup>, ion milling <sup>18</sup>, but there is always a trade-off between smallest achievable feature size, density of particles, and throughput of

fabrication. Large-area patterning up to several square centimeters with sub-20 nm features is needed to study quantum electronic and chemical properties. Moreover, many physical and chemical and optical characterization tools, such as X-ray diffraction, X-ray photoelectron spectroscopy, and X-ray topography require large ensembles of identical nanoparticles to obtain sufficient signal-to-noise ratio.

Extreme ultraviolet interference lithography (EUV-IL) has the throughput and simplicity advantages of interference lithography as well as high resolution due to its short wavelength of 13.5 nm. Generation of sub-10 nm structures has been demonstrated using EUV-IL, which is currently the record for photolithography <sup>19</sup>. Dot arrays can either be achieved using four-beam interference lithography <sup>20, 21</sup> shown in Fig. 1(a) or using achromatic Talbot lithography (ATL), also known as achromatic spatial frequency multiplication method (ASFM) <sup>22, 23</sup> shown in Fig. 1(b). Here, we employ these holographic lithography approaches using EUV light to achieve large-area dot arrays with high resolution over large areas and with superior uniformity. For this purpose, we have introduced new concepts for the fabrication of masks, i.e. diffractive transmission gratings, using EBL and nickel electroplating (Fig. 1(c)). We designed masks that are highly efficiency and require minimum number of lithographic steps to increase the yield and throughput of fabrication. We fabricated different masks and compared the performance of various approaches of multiple-beam EUV-IL and EUV-ATL. We developed an approach of EUV-ATL that produces sub-20 nm feature size over an area of

$500 \times 500 \mu\text{m}^2$  in a single-shot exposure of few seconds with high replication and throughput. Step-and-repeat exposure to stitch multiple fields is demonstrated to achieve patterned area up to several square centimeters within few minutes.

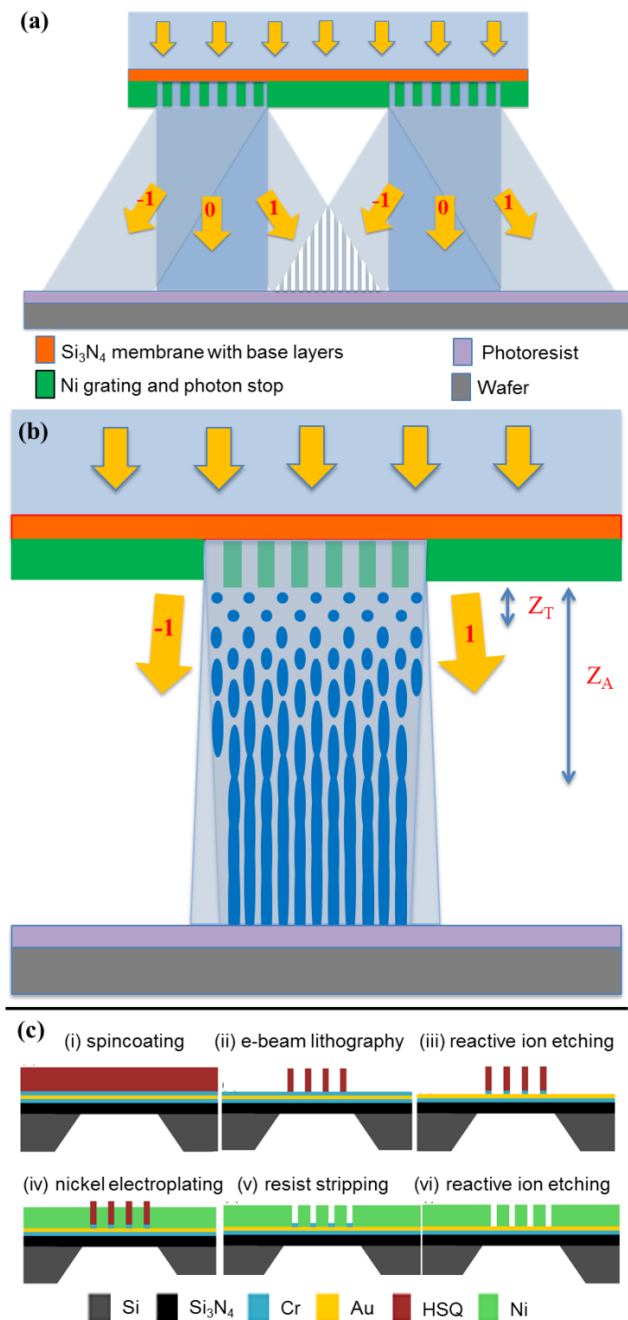


**Fig. 1** (a) Schematic of multiple-beam interference lithography showing cross-section of the mask and two interfering beams. Diffracted beams interfere and form a periodic aerial image on the wafer plane. Only first-orders and zeroth-order diffraction are shown for simplicity. (b) Schematic showing achromatic Talbot lithography and cross-section of mask. Self-images of grating are produced at the Talbot distances  $Z_T$  from the transmission mask, which starts to smear out at large distances and eventually becomes stationary at a distance larger than  $Z_A$ . (c) Schematic showing different steps for fabrication of transmission masks using nickel for grating and photon stop.

## B. Results and discussion

### Mask fabrication for EUV-IL employing nickel

EUV-IL typically involves a scheme with a mask which is illuminated with a spatially coherent EUV beam, producing a periodic aerial image at a certain distance behind the mask due to interference of diffraction orders (Fig. 1(a)). Several challenges are associated with mask fabrication towards the goal of achieving high-resolution nanoparticle arrays with uniformity over a large area in a single shot EUV exposure. Mask fabrication is done using EBL, since precise positioning of individual gratings is necessary to achieve the desired phase relations<sup>24</sup>. Complex mask fabrication strategies, which involve multiple EBL steps with overlay exposures substantially, decrease the yield of mask fabrication on thin and fragile membranes. Efficiency of transmission masks and uniformity of EUV exposure are largely dependent on the material used for mask fabrication on Si<sub>3</sub>N<sub>4</sub> membranes. A material with high diffraction efficiency is needed for gratings and a material with high attenuation to EUV light, subsequently called a photon stop, is required in the areas surrounding the gratings.

Hydrogen silsesquioxane (HSQ) is a high-resolution negative-tone EBL resist<sup>25,26</sup>. Upon exposure to electrons and photons it is converted to SiO<sub>2</sub>. It has the advantage that diffractive grating patterns can be directly written on the membranes using EBL without any pattern transfer, which reduces the number of process steps and increases the yield of fabrication. In addition, HSQ has high diffraction efficiency for EUV with a maximum efficiency at a thickness of 250 nm corresponding to an 180° phase shift in the material, as seen in Fig. 2. We note that although the diffraction efficiencies shown in Fig. 2 are for the grating period,  $p=150$  nm, these calculations are valid for all periods in present study since  $p \gg \lambda$ , the wavelength of EUV light. For grating period below 100 nm the diffraction efficiencies change with varying period<sup>19</sup>.

Nickel has been used in the fabrication of Fresnel zone plates due to its high diffraction efficiency and high-contrast at EUV and soft X-ray ranges<sup>27,28</sup> and we have introduced it for gratings in transmission masks. Moreover, a nickel layer thickness of just 120 nm gives sufficient attenuation to act as a very good photon stop, which is much higher than HSQ and almost ten times higher than conventional photon stop materials such as gold of the same thickness (at 13.5 nm wavelength, the attenuation length is 14.8 nm for nickel and 20.8 nm for gold). We also observed that nickel has constant and still fairly high diffraction efficiency above the thickness of just 100 nm (Fig. 2). This makes a 120-nm-thick nickel film suitable for photon stop, due to its high absorbance, and for diffraction gratings as it is not sensitive to variation of the layer thickness over large area. Use of such thin layers also lowers the stress of electroplated thin films, a requirement because of the fragile nature of Si<sub>3</sub>N<sub>4</sub> membranes. We fabricated masks with HSQ and nickel and present the results of EUV-IL used in this work to achieve large-area and uniform dot arrays with different interference schemes.

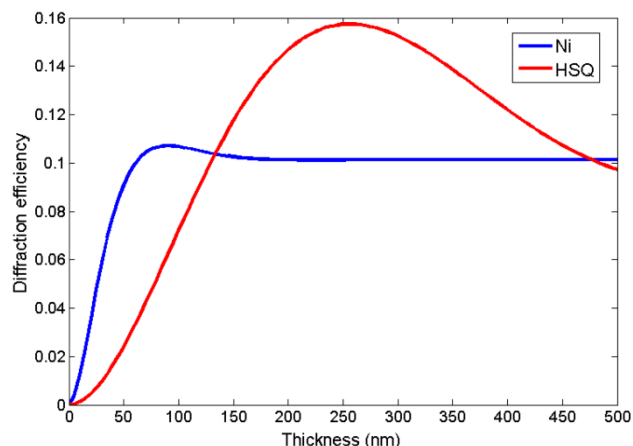


**Fig. 2** Calculated diffraction efficiency at 13.5 nm wavelength for 1:1 lines/space gratings of HSQ and nickel as a function of grating thickness for a pitch of 150 nm.

#### Four-beam EUV-IL for homogenous single-shot patterning

Two-dimensional periodic patterns consisting of dot arrays are obtained by illuminating a transmission mask consisting of four gratings. In the case when each of the gratings have the same period, interference of first-order diffracted beams from the gratings leads to the formation of two-dimensional patterns in the form of a square lattice with a period equal to  $1/\sqrt{2}$  of the period of gratings in the transmission mask. The square lattice is also rotated by  $45^\circ$  relative to the gratings. This property of demagnification is advantageous to achieve nanoparticles with high density. Fig. 1(a) shows the schematic of multi-beam interference involving a mask with diffractive transmission gratings. The diffracted beams interfere and form a periodic aerial image on the wafer plane. In this work, we adopted an approach in which the pitch of the vertical and horizontal gratings is slightly different and consequently, the period of resulting pattern is further reduced to a value that is  $1/2$  of the period in the transmission mask leading to much higher particle density.

In most conventional mask fabrication strategies, two different materials were used for the gratings and the photon stop which requires multiple overlay exposures with EBL – first, writing markers with a high contrast material such as gold, followed by a second step to fabricate gratings and a third step to prepare the photon stop which is the area on the membrane outside the desired gratings. We aimed to fabricate large-area masks using strategies that require only a single EBL step to simplify the mask making process and increase the throughput. One such fabrication method to achieve large-area and high-resolution transmission masks for four-beam EUV-IL is the footing strategy, which circumvents patterns collapse and increases the yield of fabrication substantially<sup>29</sup>. Fabrication of transmission mask using the footing strategy was done on the  $\text{Si}_3\text{N}_4$  membranes with a thermally evaporated Cr/Au/Cr layer multilayer as base layer and nickel as photon stop. EUV exposure performed with this mask results in patterns that exhibit substantial inhomogeneity (S1 in supporting information). We attribute this inhomogeneity to HSQ gratings, which are vulnerable to thickness variations since HSQ has fluctuating diffraction efficiency at around 250 nm thickness (Fig. 2). Inhomogeneous exposure from these line arrays as linear gratings leads to disparity in the shape and size of the

patterns. This makes the footing strategy disadvantageous for applications where the goal is to have high uniformity of particle sizes over large areas to study size-dependence behavior. Based on this observation, we introduce a new fabrication strategy that also involves a single EBL step but opens up the area between the gratings and employs the advantages of nickel as a material for gratings and photon stop.

Fig. 1(c) shows the schematic for the fabrication of transmission masks with nickel. In the first stage, HSQ resist was spin-coated on the  $\text{Si}_3\text{N}_4$  membrane with thermally evaporated base multilayers of Cr/Au/Cr layers (Fig. 1(c)-i). The second stage involves writing gratings using the EBL tool. The EBL exposure parameters were designed with accurate proximity effect correction and the exposure dose was optimized to suppress any possibility of footing lines to appear between the desired gratings. Following the development of the resist, gratings with 50% duty cycle were achieved with no residual HSQ in between the gratings, which is critical for subsequent stages (Fig. 1(c)-ii). In the next stage, one chromium layer was etched to expose the underneath gold layer (Fig. 1(c)-iii). Electroplating had to be optimized so that the growth of nickel on the gold layer begins simultaneously within the gratings and in the area outside the grating for photon stop. A 120-nm-thick nickel layer was electroplated (Fig. 1(c)-iv), which is sufficient for constant diffraction efficiency in case of gratings and high attenuation to EUV as a photon stop (Fig. 2). Following this step, the HSQ gratings were stripped in buffered hydrofluoric acid (HF) solution, which exposes the base chromium layer (Fig. 1(c)-v). The final stage involved removing this chromium layer to achieve transmission masks on  $\text{Si}_3\text{N}_4$  membrane with nickel central stop and clear nickel grating (Fig. 1(c)-vi).

Fig. 3(a) shows a low magnification SEM image of a mask fabricated using this new approach. The mask was designed for four-beam EUV-IL such that the interference pattern is obtained in the projected area between the gratings. SEM image at higher magnification (Fig. 3(b)) shows an area of these distinct nickel grating with a periodicity of 400 nm and the nickel photon stop, both electroplated simultaneously to a thickness of 120 nm. EUV exposures were performed on HSQ resist using this mask resulting in 2D patterns shown in Fig. 3(c) to Fig. 3(f). The SEM images in Fig. 3(c) and Fig. 3(d) show the case with low EUV exposure dose where dot arrays were obtained; whereas Fig. 3(e) and Fig. 3(f) show hole arrays resulting from high-dose exposures. As clearly seen in the low-magnification SEM images, we obtained homogenous and uniform dot and hole arrays over the full exposure area of  $400 \times 400 \mu\text{m}^2$  in a single shot exposure, which is a significant improvement compared to results obtained with the mask fabricated with footing strategy. In addition, the required EUV dose on mask using the footing strategy was  $2000 \text{ mJ/cm}^2$  for the smallest feature size of 40 nm whereas the mask with Ni electroplating yielded the same patterns with 10 times lower dose ( $200 \text{ mJ/cm}^2$ ). Thus masks using nickel gratings provide highly uniform patterning with a much faster single shot exposure time of only a few seconds to achieve the same feature size and this facilitates taking control of particle size.

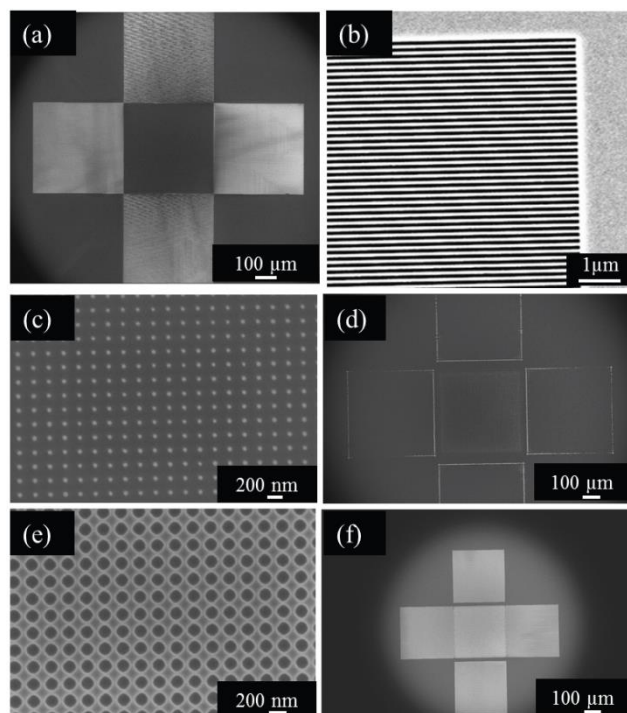


**Fig. 3** (a) SEM image of four-beam transmission mask on 100 nm thick  $\text{Si}_3\text{N}_4$  membranes consisting of nickel grating and photon stop. (b) The SEM image at higher magnification shows nickel grating with a periodicity of 400 nm and an area of the nickel central stop. The SEM images (c)-(f) are exposure results on HSQ resist using this transmission mask. (c) and (d) show high and low magnification results respectively at low dose which gives uniform 30 nm dot array with period 200 nm. (e) and (f) show high and low magnification results, respectively, at a high dose which results in 175 nm hole-array with period 200 nm. The mask is highly efficient and the resulting first order diffraction patterns is extremely uniform over  $400 \mu\text{m} \times 400 \mu\text{m}$  area.

### EUV-IL using ATL for uniform large-area patterning

In the scheme involving four-beam EUV-IL, the size of the desired area with first order diffraction patterns is limited by the main writing field size of EBL during mask fabrication. Expanding these patterns to an area of a few square millimeters is not feasible in a single shot exposure. Moreover, multi-beam interference lithography uses the incident beam ineffectively since the area of the first order diffraction patterns is much smaller than the area occupied by the gratings in the transmission mask (Fig. 1(a)). A major portion of the transmitted beam is channelled to unused diffraction orders by the gratings and this can have only limited applications<sup>30</sup>. The incident EUV beam is a Gaussian beam of limited size (FWHM of  $\sim 1.5 \text{ mm} \times 2.5 \text{ mm}$ ), which also limits the uniformly exposed area in single shot EUV exposure. Stitching of multiple fields is also not feasible due to the presence of

noninterfering diffraction orders, as seen in the schematic in Fig. 1(a) and in the SEM images of exposure results in Fig. 3(d) and 3(f). The zeroth-order diffraction patterns surround the desired first order diffraction pattern on all four sides limiting any possibility to stitch multiple first order diffraction fields over a large area.

ATL was, therefore, considered as a better approach to bypass these limitations of four-beam interference lithography for large-area patterning. ATL method makes use of Talbot effect<sup>31, 32</sup>, which is a well-known phenomenon in which illuminated objects with periodic transmission profile produce self-images at certain distances. When a periodic grating with period  $p$  is illuminated by coherent light of wavelength  $\lambda$ , self-images are formed at multiples of Talbot distance  $Z_T = p^2/\lambda$ , (Fig. 1(b)). Each subsequent self-image is laterally shifted by half the periodicity. The concept of generation of self-images at Talbot distance is applicable to lithography<sup>33</sup>, sometimes also referred to as coherent diffraction lithography<sup>34</sup>, but these techniques are limited by the depth of focus. The sample and the transmission mask need to be placed very close to each other with extreme high accuracy to record nanometer-scale patterns. To overcome this limitation, the approach of ATL was adopted which uses the spectral distribution of the EUV light to its advantage. Due to the bandwidth  $\Delta\lambda$ , the Talbot distance shifts to  $Z_T = 2np^2/\lambda \pm \Delta\lambda$ , where  $n$  is an integer, at every following self-image. This leads to a smearing and overlap of the self-images which gives rise to a stationary intensity pattern beyond the achromatic Talbot distance  $Z_A = 2p^2/\Delta\lambda$  (Fig. 1(b)). The intensity pattern on the substrate beyond the distance  $Z_A$  from the transmission mask is independent of the  $z$  position. This method is also called achromatic frequency multiplication since the aerial image has higher spatial frequency than that of the illuminated grating. For 1D and 2D gratings the period of the aerial image is reduced by factor 2 and  $\sqrt{2}$ , respectively. In addition, in this method all the intensity transmitted through the mask contributes the aerial image and therefore the pattern formation is achieved at relatively low doses. Another major advantage of using ATL is the self-healing property<sup>35, 36</sup>. This self-restoring property spreads the localized defects of the periodic gratings to the entire wavefront due to diffraction and, after several self-imaging lengths  $Z_T$ , small deformities in the periodic diffraction pattern are either invisible or weakly visible depending on the size of the perturbations. This self-imaging effect performs filtering of the high spatial frequencies from the mask and, thus, making EUV exposure results immune to surface defects and edge roughness of mask. Most importantly for our specific applications, the absence of any patterns outside this area opens up the possibility to stitch multiple EUV exposures for large area patterning.

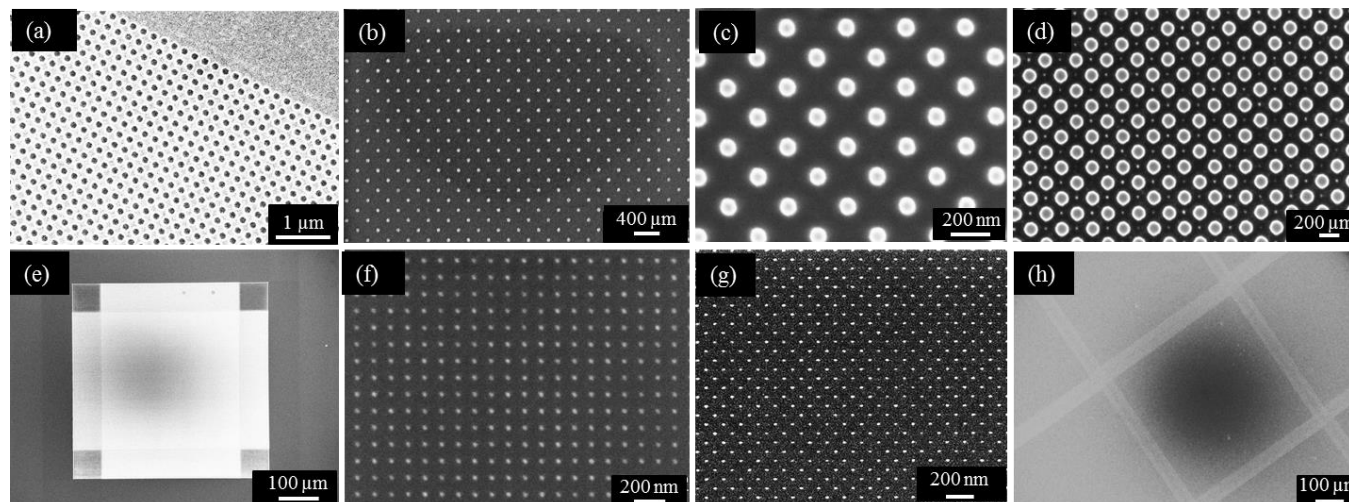


**Fig. 4** (a) SEM image of a  $\text{Si}_3\text{N}_4$  transmission mask with holes in nickel, having 150 nm period and employing EUV-ATL, obtained using the fabrication strategy shown in Fig. 1(c). SEM images of resulting patterns on EUV exposure using this high-resolution larger-area transmission mask are shown in (b) to (h). SEM image in (b) shows 35 nm HSQ dots and (c) shows 80 nm dots on silicon wafer obtained at low and high EUV exposure dose respectively. SEM image in (d) shows 130 nm dots at much larger dose together with evolution of second order diffraction patterns. SEM image in (e) is obtained at low magnification showing uniformity over an area of  $500 \times 500 \mu\text{m}^2$ . SEM image in (f) shows 15 nm dots with 100 nm period which was the smallest feature size with uniformity over full exposure area. SEM image in (g) shows the exposure on thin platinum film. The SEM image in (h) demonstrates stitching of multiple fields over  $1 \times 1 \text{ cm}^2$  area using step-and-repeat EUV exposure with a small non-interfering area between each single-shot exposure.

In this study we have adopted ATL with step and repeat strategy to cover large areas. Compared to beam scanning techniques<sup>37</sup>, the present method has its advantages. Beam scanning technique is stitching-free which is an upside but nevertheless entails averaging of beam profile over large area increasing exposure time and the exposure field is limited by the mask area on thin  $\text{Si}_3\text{N}_4$  membranes where patterning of line arrays upto  $5 \times 5 \text{ mm}^2$  has been shown in previous work. Mask fabrication above the main writing field size of EBL often has challenges and this exacerbates for 2D patterns such as hole or dot arrays. With step-and-repeat ATL, the exposure is not limited in size and can provide uniform single shot exposure for masks in the dimension of fabrication capabilities. In summary, ATL with step-and-repeat exposure uses the beam intensity and size effectively for single-shot exposure and enables stitching of multiple fields. These aspects make this method particularly advantageous for high throughput fabrication over large areas, where small field stitching errors are not important

The main challenge in ATL is the difficulty to design periodic patterns in transmission masks and to obtain high-resolution, sub-20 nm particle sizes upon EUV exposure. 2D gratings such as holes arrays are required in transmission masks to produce dot arrays. For high yields of mask fabrication on  $\text{Si}_3\text{N}_4$  membranes, we first employed a strategy to write hole-arrays over an area of  $500 \times 500 \mu\text{m}^2$ , which is the maximum writing field of our EBL tool, in HSQ resist and use this directly as masks. Since HSQ is a negative tone resist with low sensitivity, this process involves long EBL writing times and therefore it is

a low throughput process for mask fabrication. On the other hand, it involves no further fabrication step which increases the yield of fabrication. Similar to the EUV exposure results obtained using the four-beam masks with HSQ footing (S2 in supporting information); the resulting patterns in this case were also non-uniform due to the thickness variations of HSQ gratings leading to fluctuations in diffraction efficiency over such large area. For uniformity in EUV exposures with ATL, we fabricated large-area masks with hole-array pattern in nickel using the approach introduced in the schematic shown in Fig. 1(c). Instead of writing line arrays, as done previously to achieve four-beam nickel grating, we optimized the EBL parameters to obtain HSQ dot-arrays on the  $\text{Si}_3\text{N}_4$  membrane. The EBL writing and resist development parameters were calibrated so that there was no residual HSQ between the dots. The HSQ dot arrays were spread over an area of  $500 \times 500 \mu\text{m}^2$ . Following subsequent steps, we successfully fabricated several transmission masks for ATL reaching periodicity of hole-arrays in nickel down to 150 nm as shown in Fig. 4 (a).

The resulting SEM images on EUV exposure using ATL are seen in Fig. 4 (b)-(h). As mentioned, for 2D gratings such as hole arrays, the aerial image has a period equal to  $1/\sqrt{2}$  of the grating period and rotated by  $45^\circ$  and therefore the patterns have a period of 106 nm for the mask with hole-arrays with 150 nm periodicity. Fig. 4(b) and Fig. 4(c) show SEM images of fabricated nanostructures using low and high dose, respectively, demonstrating the capability to achieve different features sizes using the same mask by varying the EUV exposure dose. Additional small dots due to the second-order diffraction effects

in Talbot phenomenon become visible at higher EUV dose (Fig. 4(d)), which have a very low intensity and therefore are suppressed at low doses. This sets an upper limit of achievable single-sized dots. Single-shot EUV exposure using the mask with smallest periodicity of 150 nm also shows uniformity over the complete area of first order diffraction (Fig. 4(e)). A small non-interfering area is seen on the four sides of the pattern due to the diffraction angle of EUV light as shown in the schematic of Fig. 1(b). The width of this area is dependent on the distance of the wafer from the mask. The minimum width of the non-interfering area can be calculated for the achromatic Talbot distance as  $2p(\lambda/\Delta\lambda)$ , which is  $50 \times p$  for 4% bandwidth of the EUV light source. For the mask with an area of  $500 \times 500 \mu\text{m}^2$  and period of 150 nm, the first order diffraction patterns are formed over the area of  $485 \times 485 \mu\text{m}^2$ ; with the minimum width of the non-interfering area lost on each of the four sides being 7.5  $\mu\text{m}$ . The gap between the wafer and mask was kept much larger to show a pronounced effect of this effect as seen in the SEM image in Fig. 4(e). Uniformity over the complete first order diffraction area is a substantial improvement over the exposure results observed using masks with holes in HSQ and the corresponding SEM image at higher magnification is seen in Fig. 4(f). These masks are highly efficient and a single-shot exposure at less than  $300 \text{ mJ/cm}^2$  EUV dose results in 15 nm dot arrays with about 100 nm period on silicon rendering a density in the range of  $10^{10}$  particles/ $\text{cm}^2$  (Fig. 4(f)).

For pattern transfer to obtain metal nanoparticles, spin-coating of HSQ resist is needed on thin metal films which often has challenged associated with the adhesion of the two layers. We used intermediate adhesion layers and optimized the thicknesses to achieve 15 nm HSQ dot arrays on platinum film (Fig. 4(g)). This demonstrates that the same exposure results can be achieved on thin films of different metals and patterns can be transferred to obtain metals nanoparticles over a large area. Since a single-shot exposure required only a few seconds to achieve patterning over an area of about  $500 \times 500 \mu\text{m}^2$ , large area patterning was optimized using step-and-repeat exposure. 15 nm dot arrays over an area of  $1 \times 1 \text{ cm}^2$  were obtained in just about 5 minutes by stitching multiple fields (Fig. 4(h)). The ability to obtain large area patterns at this rate, which is about 1000 times faster than the vector-scan direct writing EBL tool, opens up the possibility to fabricate reproducible model systems consisting of nanoparticle arrays with very high-throughput.

## C. Materials and methods

### Electron beam lithography and mask fabrication

For each mask fabrication strategy, a 100-nm-thick  $\text{Si}_3\text{N}_4$  membrane was used with thermally evaporated Cr/Au/Cr multilayers having thickness of 2/5/5 nm, respectively. The first chromium layer was needed for adhesion of gold, which acts as the base for nickel electroplating. The second chromium layer provides good adhesive layer for the HSQ resist (FOX 16, Dow Corning), which was spin-coated on this membrane at 2500

rpm to achieve a thickness of 250 nm. EBL was subsequently performed to write the desired gratings using Vistec EBP 5000PlusES tool. The maximum area of exposure (main writing field size) of the EBL tool is around  $500 \times 500 \mu\text{m}^2$ . Development of resist was performed in a NaOH buffered developer (MICROPOSIT™ 351, Rohm and Hass, diluted 1:3 in water) which was then rinsed with deionized water and dried with nitrogen stream.

Plasma etching of chromium films was carried out using chlorine-based reactive ion etching for duration of 30 seconds. Nickel electroplating was done for 2 minutes to achieve layer thickness of 120 nm, at a rate of 60 nm per minute. This process was optimized for uniform growth between the nanostructures and the surrounding areas (as photon stop) with low stress on the membranes. The bath temperature was maintained at 58 °C at a pH value of 3. The peak current was maintained at 30 mA pulsed with a duty cycle of 90%. Electroplating rate was calibrated for a low value to reduce the stress on the membranes during the growth of nickel and for uniformity of the layer. Following the electroplating process, HSQ is removed in 1:7 buffered oxide etch (BOE or buffered HF) solution for 150 seconds.

### EUV interference lithography

EUV-IL exposures were carried out at the XIL-II beamline of Swiss Light Source (SLS), Paul Scherrer Institute, Switzerland. The synchrotron light from the undulator is spatially coherent EUV light of 13.5 nm wavelength (91.85 eV) and 4% bandwidth ( $\Delta\lambda/\lambda$ ). A silicon wafer was spin-coated with 45-nm-thick HSQ resist (XR-1541, Dow Corning) at 4500 rpm for 120 seconds. The transmission mask fabricated using one of the different strategies was mounted between the EUV light source and the spin-coated silicon wafer. The distance between the mask and the wafer was calculated depending on the lithography technique used and the value from design of the interference masks. For the four-beam EUV exposures in the experiments, this gap value was set at 11.85 mm. Masks using ATL require this distance to be larger than the achromatic Talbot distance and patterning become independent in z-position. The gap value was set at 1.5 mm for HSQ and nickel masks generating dots with a periodicity of 212 nm, while the high resolution nickel mask generating periodicity of 100 nm had a gap value of 1 mm for EUV exposure in Fig 1(e) to show pronounced non-interfering area and 0.5 mm for the step-and-repeat exposure in Fig 1(h). The exposure dose was varied in order to cover the whole exposure latitude, i.e. obtaining nanoparticles with the smallest and largest achievable size using the same mask on the same wafer. The exposure dose in all cases was varied from  $100 \text{ mJ/cm}^2$  to  $3000 \text{ mJ/cm}^2$  to cover the full spectrum of particle size. Following EUV exposures, the samples were developed in the NaOH-based developer for 30 seconds.

### Instrumentation and simulations

Calculation of the diffraction efficiency for different material at 13.5 nm wavelength was done using a rigorous coupled wave analysis (RCWA) method. The duty cycle of the gratings was set at 50%. For analysis of masks during different stages of fabrication and to study the EUV exposure results, optical microscopy was done in conjunction with a scanning electron microscopy (Zeiss Supra VP55).

## Conclusions

We have established an effective lithographic approach for fabricating well-defined model systems for studying ordered nano-sized particles which are densely packed over large areas. Although the footing strategy reduces the electron beam writing steps, it compromises on the efficiency of these masks and uniformity for exposure over a large area. We have successfully implemented a novel mask fabrication strategy with one-step EBL and nickel as grating material and central stop which results in highly efficient masks. We have demonstrated that nickel masks are the most efficient for large area uniform exposure. In comparison to masks using four-beam interference, ATL is found to be the most effective technique to achieve large area nanostructures. We obtained 15 nm dot-arrays with periodicity of about 100 nm over an area of around  $500 \times 500 \mu\text{m}^2$  in a single shot exposure which can be replicated over more than  $1 \times 1 \text{ cm}^2$  area using step-and-repeat exposures in a matter of few minutes.

High-resolution patterns generated using ATL guarantee good signal-to-noise ratio when used in characterization techniques in catalysis research, spectroscopy, optics and magnetics. We have used these properties to achieve small feature sizes with uniformity over large areas and with complete control over particle size. We optimized the adhesion layer to demonstrate patterning on thin platinum film and different metal nanoparticles can be achieved by HSQ pattern transfer to metal films. Further studies aim for feature sizes well below 10 nm with much higher density (resolution below 100 nm) over square centimeter large area.

## Acknowledgements

We thank Michaela Vockenhuber and Vitaliy Guzenko for their technical support in using the EUV lithography tool and the electron beam lithography tool, respectively. Part of this work was performed at Swiss Light Source (SLS), Paul Scherrer Institute, Switzerland. The PSI Research Commission is greatly acknowledged for financial support through its CROSS program.

## Notes and references

Corresponding authors:

\* [yasin.ekinci@psi.ch](mailto:yasin.ekinci@psi.ch), \*\* [jeroen.vanbokhoven@chem.ethz.ch](mailto:jeroen.vanbokhoven@chem.ethz.ch)

<sup>a</sup> Laboratory for Micro and Nanotechnology, Paul Scherrer Institute, 5232 Villigen-PSI, Switzerland.

<sup>b</sup> Institute for Chemical and Bioengineering, ETH Zurich, Switzerland.

<sup>c</sup> Electrochemistry Laboratory, Paul Scherrer Institute, 5232 Villigen-PSI, Switzerland.

<sup>d</sup> Department of Chemistry, Carl von Ossietzky Universität Oldenburg, 26111 Oldenburg Germany.

<sup>e</sup> Laboratory of Physical Chemistry, ETH Zurich, Switzerland.

<sup>f</sup> Laboratory for Catalysis and Sustainable Chemistry, Paul Scherrer Institute, 5232 Villigen-PSI, Switzerland.

Electronic Supplementary Information (ESI) available: [Multiple-beam EUV interference lithography using HSQ gratings with footing (S1); EUV-IL using ATL with HSQ gratings (S2)]. See DOI: 10.1039/b000000x/

1 P. V. Kamat, *J. Phys. Chem. B*, 2002, **106** (32), 7729–7744.

- 2 K. L. Kelly, E. Coronado, L. L. Zhao and G. C. Schat, *J. Phys. Chem. B*, 2003, **107** (3), 668–677.
- 3 M. A. El-Sayed, *Acc. Chem. Res.*, 2001, **34** (4), 257–264.
- 4 X. Lu, M. Rycenga, S. E. Skrabalak, B. Wiley and Y. Xia, *Annu. Rev. Phys. Chem.*, 2009, **60**:167–92.
- 5 Y. Sun and Y. Xia, *Science*, 2002, **298**, 2176.
- 6 T. Hyeon, *Chem. Commun.*, 2003, 927–934.
- 7 K. Jain, M. Zemel, M. Klosner, *Proceedings of the IEEE*, 2002, **90**(10), 1681–1688.
- 8 A. L. González, C. Noguez, J. Beránek and A. S. Barnard, *J. Phys. Chem. C*, 2014, **118** (17), 9128–9136.
- 9 I. M. Billas, A. Châtelain and W. A. de Heer, *Science*, 1994, **265**(5179), 1682–1684.
- 10 A. Rabis, P. Rodriguez and T. J. Schmidt, *ACS Catalysis*, 2012, **2** (5), 864–890.
- 11 N. M. Markovic, T. J. Schmidt, V. Stamenkovic, and P. N. Ross, *Fuel Cells*, 2001, **1**, 105–116.
- 12 J. A. van Bokhoven, *Chimia*, 2009, **63**, 257–260.
- 13 E. Bus, R. Prins, and J. A. van Bokhoven, *Catal. Commun.*, 2007, **8**, 1397–1402.
- 14 J. Grunes, J. Zhuab and G. A. Somorjai, *Chem. Commun.*, 2003, **18**, 2257–2260.
- 15 R. Prins, M. Schildenberger, Y. C. Bonetti and J. Gobrecht, *Chimia*, 2000, **54**(1-2), 63–65(3).
- 16 J. Grunes, J. Zhu, E. A. Anderson and G. A. Somorjai, *J. Phys. Chem. B*, 2002, **106** (44), 11463–11468.
- 17 S. Kwon, X. Yan, A. M. Contreras, J. A. Liddle, G. A. Somorjai and J. Bokor, *Nano Lett.*, 2005, **5**(12), 2557–62.
- 18 S. Wang, G. J. Yu, J. L. Gong, D. Z. Zhu and H. H. Xia, *Nanotechnology*, 2007, **18**, 015303.
- 19 B. Päivänranta, A. Langner, E. Kirk, C. David and Y. Ekinci, *Nanotechnology*, 2011, **22**(37), 375302.
- 20 V. Auzelyte, C. David and H. H. Solak, *J. Micro/Nanolith. MEMS MOEMS.*, 2009, **8**(2), 021204.
- 21 H. H. Solak, C. David, J. Gobrecht, L. Wang and F. Cerrina, 2002, **61–62**, 77–82.
- 22 H. H. Solak and Y. Ekinci, *J. Vac. Sci. Technol. B*, 2005, **23**, 2705.
- 23 L. Wang, B. Terhalle, M. Hojeij, V. A. Guzenko and Y. Ekinci, *J. Vac. Sci. Technol. B*, 2012, **30**, 031603.
- 24 H. H. Solak, C. David, J. Gobrecht, L. Wang and F. Cerrina, *J. Vac. Sci. Technol. B*, 2002, **20**, 2844.
- 25 H. Namatsu, T. Yamaguchi, M. Nagase, K. Yamazaki and K. Kurihara, *Microelectronic Engineering*, 1998, **41–42**, 331–334.
- 26 I. Junarsa, M. P. Stoykovich, P. F. Nealey, Y. Ma, F. Cerrina and H. H. Solak, *J. Vac. Sci. Technol. B*, 2005, **23**, 138.
- 27 E. D. Fabrizio, F. Romanato, M. Gentili, S. Cabrini, B. Kaulich, J. Susini and R. Barrett, *Nature*, 1999, **401**, 895–898.
- 28 J. Reinspach, M. Lindblom, M. Bertilson, O. von Hofsten, H. M. Hertz and A. Holmberg, *J. Vac. Sci. Technol. B*, 2011, **29**, 011012.
- 29 L. Wang, D. Fan, V. A. Guzenko and Y. Ekinci, *J. Vac. Sci. Technol. B*, 2011, **31**, 06F602.
- 30 T. Siegfried, Y. Ekinci, H. H. Solak, O. J. F. Martin, and H. Sigg, *Appl. Phys. Lett.*, 2011, **99**, 263302
- 31 H. Talbot, *Philosophical Magazine Series 3*, 1836; **9**(56), 401–407.
- 32 K. Paturski and E. Wolf, *Elsevier Science Publishers*, 1989, **27**, 2–108.

## ARTICLE

- 33 D. C. Flanders, A. M. Hawryluk and H. I. Smith, *J. Vac. Sci. Technol.*, 1979, **16(6)**, 1949-1952.
- 34 C. Zanke, M. Qi and H. I. Smith, *J. Vac. Sci. Technol. B*, 2004, **22**, 3352.
- 35 A. W. Lohmann, J. A. Thomas, *Applied Optics*, 1990, **29(29)**, 4337-4340.
- 36 X. Da, *Applied Optics*, 1992, **31(16)**, 2983-2986.
- 37 L. Wang, H. H. Solak and Y. Ekinici, *Nanotechnology*, 2012, **23**, 305303 (5pp)